Check for updates

Ensemble averaged structure–function relationship for nanocrystals: effective superparamagnetic Fe clusters with catalytically active Pt skin†

Valeri Petkov, [iD] *[a] Binay Prasai,[a] Sarvjit Shastri,[b] Hyun-Uk Park,[c] Young-Uk Kwon [iD] [c] and Vassil Skumryev[d,e]

Practical applications require the production and usage of metallic nanocrystals (NCs) in large ensembles. Besides, due to their cluster–bulk solid duality, metallic NCs exhibit a large degree of structural diversity. This poses the question as to what atomic-scale basis is to be used when the structure–function relationship for metallic NCs is to be quantified precisely. We address the question by studying bi-functional Fe core–Pt skin type NCs optimized for practical applications. In particular, the cluster-like Fe core and skin-like Pt surface of the NCs exhibit superparamagnetic properties and a superb catalytic activity for the oxygen reduction reaction, respectively. We determine the atomic-scale structure of the NCs by non-traditional resonant high-energy X-ray diffraction coupled to atomic pair distribution function analysis. Using the experimental structure data we explain the observed magnetic and catalytic behavior of the NCs in a quantitative manner. Thus we demonstrate that NC ensemble-averaged 3D positions of atoms obtained by advanced X-ray scattering techniques are a very proper basis for not only establishing but also quantifying the structure–function relationship for the increasingly complex metallic NCs explored for practical applications.

Introduction

Most bulk metallic materials are 3D periodic at the atomic level and so their physicochemical properties appear as a sum of equivalent contributions of identical unit cells comprising a relatively small number of atoms. This greatly facilitates establishing the structure–function relationship for bulk crystalline metals and alloys employed in practical applications. Nanometer-sized metallic crystals (NCs) though are not necessarily 3D periodic at the atomic level. Hence, their physicochemical properties often appear as a combination of contributions of non-equivalent volume fractions of the NCs such as, for example, the NC surface and the interior. Furthermore,

[a]Department of Physics, Central Michigan University, Mt. Pleasant, Michigan 48859, USA. E-mail: petko1vg@cmich.edu
[b]X-ray Science Division, Advanced Photon Source, Argonne National Laboratory, Argonne, Illinois 60439, USA
[c]Department of Chemistry, Sungkyunkwan University, Suwon 16419, Republic of Korea
[d]Institució Catalana de Recerca i Estudis Avançats (ICREA), 08010 Barcelona, Spain
[e]Departament de Física, Universitat Autònoma de Barcelona, 08193 Bellaterra, Spain
†Electronic supplementary information (ESI) available: TEM and XRD data, sample preparation, experimental and modelling details. See DOI: 10.1039/c7nr05768g

reality necessitates the production and usage of metallic NCs en masse, *i.e.* in large ensembles. No matter how refined the production process is, the atomic-level structure and so the properties of some NCs belonging to such an ensemble may appear a bit different from those of the general population of NCs in the ensemble.[1–5] The intrinsic non-periodicity and likely structural diversity of as-produced and used metallic NCs pose the fundamental question as to what atomic-level basis is to be used when the relationship between their structure and functionality is to be quantified precisely. Here we demonstrate that NC ensemble-averaged positions of atoms obtained by advanced X-ray scattering techniques are very much up to the task. Indeed this may not come as a big surprise because the actual functionality of metallic NCs also appears as an ensemble-averaged quantity. In particular, we determine the 3D positions of atoms in three samples of metallic NCs composed of a cluster-like Fe core nested inside a tight skin of Pt atoms that is only one to two monolayers thick. The determination is challenging because the NCs are optimized for practical applications and so appear very small in size (2.5 nm). Besides, the NCs are highly dispersed on fine carbon powder. Moreover, Fe and Pt atoms forming the NC core and skin, respectively, have very different X-ray scattering amplitudes. This renders Fe cores hard to access by traditional

imaging and scattering techniques. Therefore, the 3D structure determination is done by non-traditional resonant high-energy X-ray diffraction (HE-XRD) coupled to element-specific atomic pair distribution function (PDF) analysis.[6–9] We find that the Fe core and Pt skin of the NCs are bcc- and fcc-type ordered, respectively, *i.e.* incommensurate in terms of packing efficiency and near atomic neighbor distribution. Regardless of their disparity, the core and the skin modulate the properties of each other significantly and advantageously. In particular, as our superconducting quantum interference magnetometry and rotating disc electrode experiments show, the NCs function both as superparamagnets and catalysts for the oxygen reduction reaction (ORR). The former renders the NCs promising for advanced biomedical applications.[10,11] The latter provides clues for bringing clean energy conversion technologies, in particular fuel cells, closer to commercialization.[12] Using streamlined DFT together with the experimental magnetic, catalytic and 3D structure data, we provide a quantitative explanation of both the long-debated cluster-size dependence of the magnetic moment of Fe atoms in clusters and the impact of Pt skin-thickness on the activity of ORR catalysts. To be more precise, we show that both effects are related to specific features of surface sites in the Fe cores and Pt skin, in particular local structural disorder and effective atomic coordination numbers, thereby demonstrating an experimental approach to establishing the structure–function relationship for ensembles of NCs in a quantitative manner, and not just establishing trends. Finally, based on the findings presented here, we argue that, to be precise, studies on metallic NCs may need to both go beyond the limits of traditional crystallography and account for the likely structural diversity in the typically large ensembles of metallic NCs explored for practical applications. The latter may be facilitated by using 3D nanostructures determined by experiment and not inferred by educated guessing.

Experimental

The Fe core–Pt skin NCs were synthesized by a one-step ultrasound-assisted polyol reaction between Fe(III) acetylacetonate, Pt(II) acetylacetonate, $Fe(C_5H_7O_2)_3$ and $Pt(C_5H_7O_2)_2$.[13] The size of the Fe core and the thickness of the Pt skin were fine-tuned so that the resulting NCs appeared with an average size of 2.5 nm. Pure Pt NCs were also synthesized and used as a reference sample. Note that Pt shell-based NCs with a size close to 3 nm have proved optimal for a number of technologically important catalytic applications, including the ORR. In addition, biocompatible and oxidation resistant, *e.g.* noble metal protected, superparamagnetic particles with an overall size of about 2–3 nm are considered very promising for biomedical applications. That is because the particles can interact with common biological entities, including genes (~2 nm), protein complexes (1 nm–5 nm) and the cell membrane (~5 nm), thereby enabling cellular therapy, magnetically guided drug delivery, magnetic resonance imaging, and

hyperthermia treatment.[14] More details of the synthesis protocol employed here can be found in the ESI.†

The overall (bulk) chemical composition of Fe core–Pt skin NCs was determined by inductively coupled plasma atomic emission spectroscopy (ICP-AES) and was found to be $Fe_{0.4}Pt$ ($Fe_{166}Pt_{421}$), $Fe_{0.7}Pt$ ($Fe_{244}Pt_{351}$) and $Fe_{1.2}Pt$ ($Fe_{336}Pt_{297}$). The size, shape and chemical pattern of Fe_xPt (x = 0.4, 0.7 and 1.2) NCs were determined by High-Angle Annular Dark-Field (HAADF) Scanning Transmission Electron Microscopy (STEM) experiments. Exemplary HAADF-STEM images are shown in Fig. 1b and S1.† As can be seen in the figures, pure Pt and Fe_xPt (x = 0.4, 0.7 and 1.2) NCs appear with an average size of 2.5(±0.3) nm, polyhedral shape and relatively well-defined facets. Besides, the NCs are well separated from each other, which is important for optimizing their functionality. Noteworthy, the NCs appear uniformly bright which, given the large difference between the atomic numbers of Fe (Z = 26) and Pt (Z = 78), indicates that their top surface is formed of Pt species alone. Elemental maps of Fe_xPt (x = 0.4, 07 and 1.2) NPs shown in Fig. 1(d–f) indicate the same. To evaluate the number of surface Pt layers we carried out simplistic calculations based on the experimental data for the bulk chemical composition and average size of the NCs, and the well-known elemental size of Fe (2.52 Å) and Pt (2.775 Å) atoms. Results showed that the Pt surface of Fe_xPt (x = 0.4, 0.7 and 1.2) NPs is about 2, 1.5 and 1 atomic layer thick, respectively, *i.e.*, "skin-like" from a morphological viewpoint. The so-obtained independent estimates for the thicknesses of Pt skin matched well the pre-desired number of Pt layers. Hence, for clarity, hereafter Fe_xPt (x = 0.4, 0.7 and 1.2) NCs are referred to as Fe@2Pt, Fe@1.5Pt and Fe@1Pt NCs, respectively.

The electronic properties of Fe and Pt atoms in Fe@Pt NCs were studied by X-ray photoelectron spectroscopy (XPS). Typical XPS Fe 2p and Pt 4f spectra are shown in Fig. 1a. As can be seen in the figure, the Fe $2p_{3/2}$ core-level peak position in Fe@1Pt, Fe@1.5Pt and Fe@2Pt NCs is shifted by (+) 0.59 eV, 0.79 eV and 1.19 eV, respectively, in comparison to the bulk value of 706.9 eV. As discussed in the ESI† and supported by independent resonant HE-XRD experiments (see Fig. 2d and S7†), the shift reflects the gradual diminishing of the size of the Fe cores with the thickness of the Pt skin.[15] On the other hand, the Pt $4f_{7/2}$ core-level peak position in Fe@1Pt, Fe@1.5Pt and Fe@2Pt NCs is shifted by (−) 0.34 eV, 0.25 eV and 0.12 eV, respectively, in comparison to the bulk value of 71.0 eV (see Fig. 1c). As discussed in the ESI† and indicated by prior studies on transition metal core–Pt shell NCs, the shift can be related to changes in the coordination environment of surface atoms in Fe@Pt NCs with the thickness and degree of structural relaxation of the Pt skin, including changes in Pt–Pt bonding distances.[15–19]

Ensemble-averaged 3D positions of atoms in Fe@Pt NCs were determined strictly adhering to the successful practices of structure studies on polycrystalline metallic materials. From a methodological point of view, this made perfect sense because determining the 3D atomic structure of both polycrystalline and nanocrystalline metallic particles relies on diffrac-
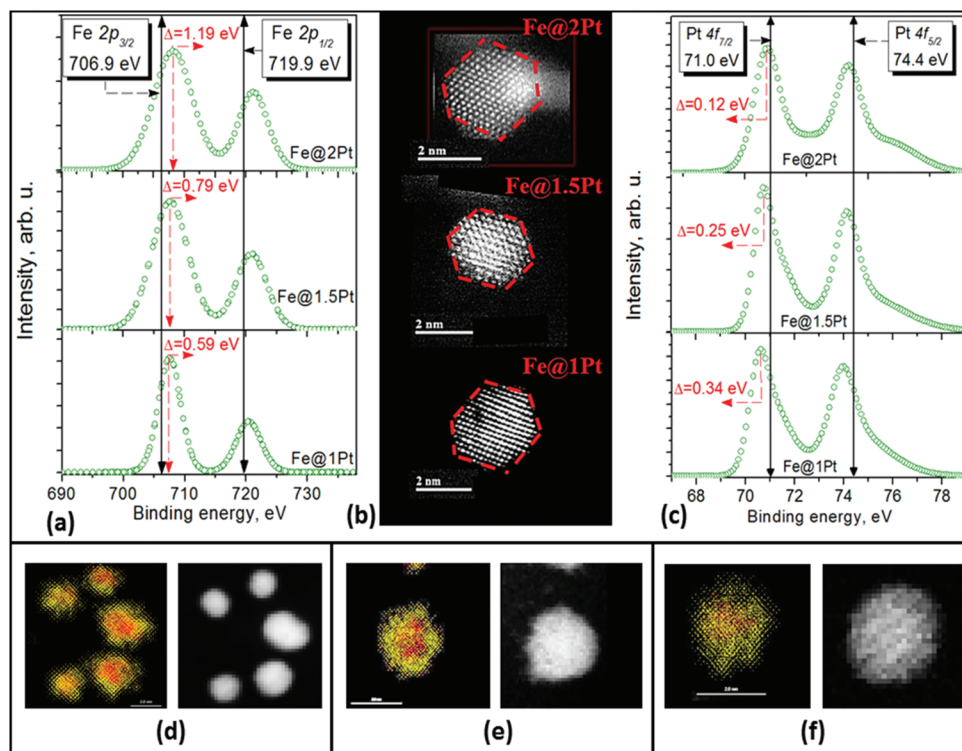
Fig. 1 (Upper panel) (a) Typical XPS Fe $2p_{/3/2}$ and $2p_{1/2}$ spectra for Fe@Pt NCs. The positive shift, Δ, of the binding energy of Fe atoms in the respective NCs (red broken lines) is evaluated with respect to the Fe $2p_{3/2}$ spectral line (black solid line) characteristic of bulk Fe. (b) Representative HAADF-STEM images of Fe@Pt NCs. Images indicate that the NCs have an average size of approximately 2.5($\pm$0.3) nm and polyhedral shape. Red broken lines outline the relatively well-defined facets of the NCs. (c) Typical XPS Pt $4f_{7/2}$ and $4f_{5/2}$ spectra for Fe@Pt NCs. The negative shift, Δ, of the binding energy of Pt atoms in the respective NCs (red broken lines) is evaluated with respect to the Pt $4f_{7/2}$ spectral line (black solid line) characteristic of bulk Pt. (Lower panel) Representative EDS elemental maps and HAADF-STEM images of (d) Fe@1Pt, (e) Fe@1.5Pt and (f) Fe@2Pt NCs. Fe atoms are in red and Pt atoms are in yellow.

tion data obtained from ensembles of entities with a fairly close chemical composition, size, and shape.[20] In particular, resonant HE-XRD experiments were conducted at the K adsorption edge of Pt. The experiments involved measuring two diffraction patterns close to but below the adsorption edge of Pt (see Fig. S4†), taking the difference between the two patterns, and Fourier transforming it into the so-called Pt-differential PDFs. The so-called Fe–Fe partial and total PDFs, including total PDFs for pure Pt and Fe particles,[21] were also obtained.[9] Details are given in the ESI† and ref. 22. The PDFs are shown in Fig. 2 and S8.† Note that unlike local-probe techniques such as extended X-ray absorption fine structure spectroscopy (EXAFS), element-specific atomic PDFs obtained by resonant HE-XRD can reveal interatomic correlations extending up to distances equal to the diameter (size) of the metallic NCs under study (see Fig. 2c and d). This greatly facilitates determining the 3D positions of atoms constituting multimetallic NCs, including the bi-metallic Fe@Pt NCs studied here. The high quality of resonant HE-XRD experiments was validated against bulk Fe and Pt standards, as shown in Fig. 2b.

Next, several plausible 3D structure models for Fe@Pt NCs were built by Molecular Dynamics (MD) based on the quantum corrected Sutton–Chen potential. To be as realistic

as possible, the models reflected the average size (~2.5 nm), shape (polyhedral) and overall chemical composition (Fe$_x$Pt, where $x = 0.4$, 07 and 1.2) of the NCs modeled. Models for pure Pt and Fe particles were also built. All models were tested against the respective total and Fe–Fe partial PDFs. As discussed in the ESI† and demonstrated in Fig. S8,† MD models featuring an fcc and bcc-type structure approached, respectively, the experimental PDFs for pure Pt and Fe particles to an acceptable level, and so were considered further. However, MD models for Fe@Pt NCs based on a structurally coherent fcc Fe core and fcc Pt skin failed the test, as data in Fig. 2a and S9† show. The failure indicated that, though exhibiting HE-XRD patterns similar to that of pure Pt NCs (see Fig. S5†), Fe@Pt NCs may not be described as stacks of close packed atomic layers known to occur with bulk fcc metals and alloys, including bulk Fe$_x$Pt alloys with $0 < x < 1.2$.[23] On the other hand, as data in Fig. 2a and S10† show, models for Fe@Pt NCs based on a bcc-type Fe core and fcc-type Pt skin reproduced the experimental PDF data reasonably well. For reference, contrary to the fcc-type structure which involves both close packed $(111)_{fcc}$ atomic layers and $<110>_{fcc}$ directions, the bcc-type structure does not involve close packed atomic layers but close packed $<111>_{bcc}$ directions alone.[24] Accordingly, the atomic
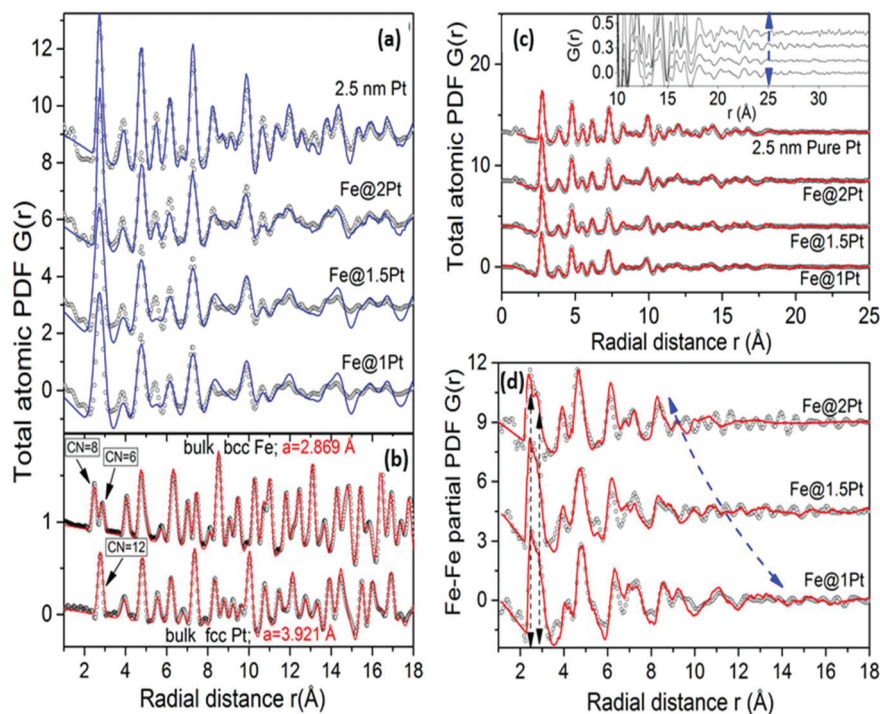
Fig. 2 (Left) (a) Experimental (symbols) and computed (blue line) atomic PDFs for pure 2.5 nm Pt and Fe@Pt NCs. The computed PDFs are derived from MD optimized models featuring close packed layers of Fe core and Pt shell atoms stacked in an fcc-type sequence. The computed PDFs fail to reproduce the experimental data, in particular in the regions from 4 Å to 8 Å and 14 Å to 16 Å. (b) Experimental (symbols) and computed (red line) atomic PDFs for bulk bcc Fe and fcc Pt. The computed PDFs are based on an infinite bcc- and fcc-type lattice with a parameter a = 2.869 Å and a = 3.921 Å, respectively. Arrows emphasize the difference between the near-neighbor coordination spheres in bcc- (8 + 6 near neighbors) and fcc-type (12 near neighbors) metals. (Right) (c) RMC fits (red lines) to the experimental (symbols) total atomic PDFs for 2.5 nm Pt and Fe@Pt NCs. The higher-r part of the experimental data is shown in the inset. Vertical broken line (in blue) marks the real-space distance at which the physical oscillations in the PDF data decay to zero. (d) RMC fits (red line) to the experimental (symbols) Fe–Fe partial PDFs for Fe@Pt NCs. Inclined broken line (in blue) emphasizes the increasing size of Fe cores with the diminishing thickness of the Pt skin. Vertical broken lines (in black) show the nearly merged first and a bit more distant second coordination spheres of Fe atoms in the cores. The RMC fits in (c) and (d) reflect the atomic structures shown in Fig. 3a. The quality factors, R_w, for the fits are in the order of 7 (±3) %.

packing fraction (68% for bcc vs. 74% for fcc) and near-neighbor distribution (8 + 6 for bcc vs. 12 for fcc; see Fig. 2b) in the bcc- and fcc-type structure are significantly different. The advantage of the bcc-type Fe@fcc-type Pt structure model over the fcc-type Fe@fcc-type Pt one becomes even more evident when Fe–Fe partial PDFs derived from the models are compared with the respective experimental data sets, as demonstrated in Fig. S11.† Hence, the former model was considered as a likely 3D atomic structure of Fe@Pt NCs. Here it may be added that the bcc and fcc characters of the atomic arrangement in the Fe core and Pt skin of Fe@Pt NCs, respectively, are consistent with our synthesis protocol, where Pt atoms are deposited on already formed cores of Fe atoms.

Third, MD models for Fe@Pt NCs found likely as described above were refined further by reverse Monte Carlo (RMC) guided by the respective total and partial Fe–Fe atomic PDFs. The bcc- and fcc-type MD models for pure Fe and Pt particles were refined as well. The refinement was necessary since nano-sized metallic particles can exhibit specific atomic-level features, such as considerable surface structural relaxation, which may not be captured well by MD alone, *i.e.* without experi-

mental input.[25] As it should be, the thermal (Debye–Waller type) and static displacements, *i.e.* relaxation, of atoms in the refined models were treated separately. Besides, the energy of the refined models was minimized further using pair-wise potentials taken from literature sources. Details of RMC computations are given in the ESI.†

Last but not the least, RMC-refined models were evaluated using a common goodness-of-fit indicator (see eqn (S26)†) and found to be of high quality. Fine structural features of the Fe core and Pt skin in Fe@Pt NCs were cross-checked by computing Fe–Fe–Fe and Pt–Pt–Pt bond-angle distributions shown in Fig. S13 and S14,† respectively. Altogether, the RMC-refined models appeared fully consistent with the experimental (i) HAADF-STEM data in terms of size and shape, (ii) EDS maps in terms of mutual distribution of Fe and Pt atoms, (iii) ACP-IES data in terms of overall chemical composition and, as shown in Fig. 2c and d, (iv) reproduced the experimental total and partial atomic PDFs data in very good detail. As such, within the limits of experimental accuracy, RMC-refined 3D atomic models shown in Fig. 3a can be considered as the most likely, ensemble-averaged 3D atomic structures of pure Pt and
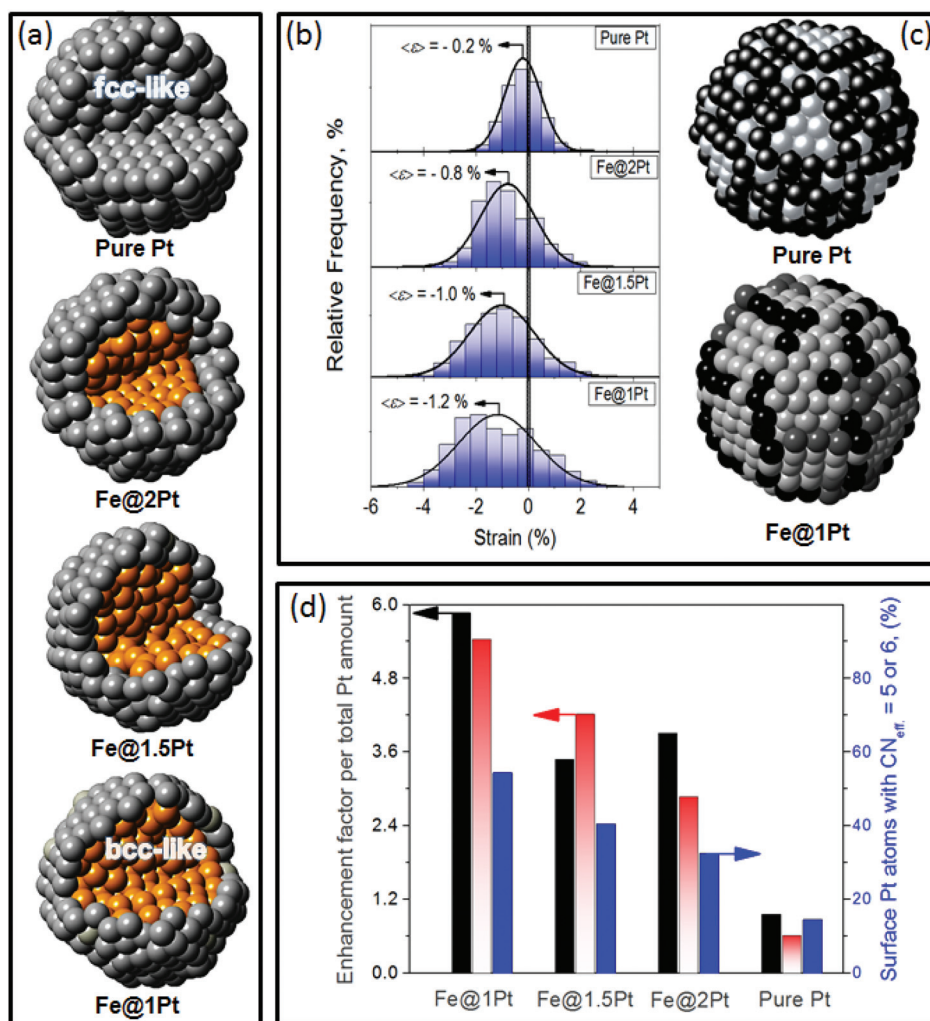
Fig. 3 (a) Full-scale structures for 2.5 nm fcc Pt and bcc Fe@fcc Pt NCs determined as described in the text. Pt atoms are in gray and Fe atoms are in light brown. Note that, on average, each Pt atom at the core@skin interface in Fe@1Pt, Fe1.5Pt and Fe@2Pt NCs has about 1.4, 1.1 and 0.5 Fe atoms as first neighbors, respectively. (b) Distribution of bonding distances between surface Pt atoms from the structures shown in (a). The distances appear "strained" when normalized (in %) against the bulk Pt–Pt bonding distance of 2.775 Å. (c) Effective coordination, CN_{eff}, for surface sites in pure Pt and Fe@1Pt NCs, as derived from the respective structures shown in (a). Five-fold and 6-fold coordinated surface Pt atoms are shown in gray. Four-fold and 3-fold coordinated surface Pt atoms are shown in black. (d) Percentage of 5-fold and 6-fold coordinated surface atoms (*vs.* all surface atoms) in pure Pt and Fe@Pt NCs (blue bars). Enhancement (red bars) of the catalytic activity of Fe@Pt NCs for ORR (*vs.* pure Pt NCs) derived as a ratio of the number of 5-fold and 6-fold coordinated surface Pt atoms alone and the total number of Pt atoms in the respective NCs. Enhancement (black bars) of the (mass) catalytic activity of Fe@Pt NCs for ORR (*vs.* pure Pt NCs) obtained by CV and RDE experiments described in the ESI.†

Fe@Pt NCs, and so are fit for their purpose.[20,25–27] That is, 3D positions of atoms in the structures can be used to assess the functionality of the respective ensembles of NCs.

The catalytic functionality of Fe@Pt NCs for the ORR was determined by cyclic voltammetry (CV) and rotating disk electrode (RDE) experiments in 0.1 M HClO₄ electrolyte at room temperature, as described in the ESI.† Exemplary CV curves and the so-called Tafel plots for pure Pt and Fe@Pt NCs are shown in Fig. S2.† For reference, without loss of generality, the ORR over the catalyst surface can be expressed as $O_2 + 4H^+ + 4e^- \rightarrow H_2O$. That is, oxygen molecules adsorbed and reduced at the surface react with protons supplied to the surface to form water. As data in Fig. S2† show, the ORR kinetics of

Fe@Pt NCs is superior to that of standard Pt NCs in the high potential range (0.88 V–0.98 V). In particular, the mass activity (MA) of pure Pt and Fe@Pt NCs for ORR, which is relevant to practical applications, increases in the order pure Pt < Fe@2Pt < Fe@1.5Pt < Fe@1Pt NCs. The improvement in the MA of Fe@Pt NCs for ORR is best illustrated in Fig. 3d. Qualitatively, it can be attributed to one or more of the following factors: (i) ligand/electronic effects arising from charge exchange between atoms at the Fe core@Pt skin interface, (ii) strain effects arising from the difference between the size of Fe and Pt atoms forming the NC core and skin, respectively, and (iii) geometric effects where particular configurations of atoms from the Pt skin appear beneficial to the ORR.[4,13] Here we show

that, though counterintuitive, the improvement is proportionate to the increase in the effective coordination number of atoms forming the Pt skin with decrease in its thickness.

The magnetic response of Fe@Pt NCs to DC and AC magnetic fields, and its change with temperature, were studied on a superconducting quantum interference (SQUID) magnetometer, as described in the ESI.† Hysteresis curves measured at 2 K are shown in Fig. S3(left).† Coercivity, H_c, values for Fe@1Pt, Fe@1.5Pt and Fe@2Pt NCs determined from the curves are 2120 Oe, 2080 Oe and 2050 Oe, respectively. Zero field and DC field (100 Oe) magnetization curves are shown in Fig. 4a. The curves exhibit a clear "blocking effect", where the

magnetic moment of the Fe cores is pinned to an easy direction of magnetization. The effect is considered a hallmark of superparamagnetism.[28] The superparamagnetic behavior of Fe@Pt NCs is also documented by the frequency-dependent "cusp" in the measured AC susceptibly curves shown in Fig. S3 (right).† The so-called "blocking temperature", T_B, for Fe@1Pt, Fe@1.5Pt and Fe@2Pt NCs was determined from the DC magnetization curves (follow the arrows in Fig. 4a) and found to be 15 K, 11 K and 8 K, respectively. For small clusters, H_c may not depend on the cluster's size significantly and T_B is expected to decrease fast with the cluster's size, so long as it is <6 nm.[28,29] Indeed, this is what we observe.
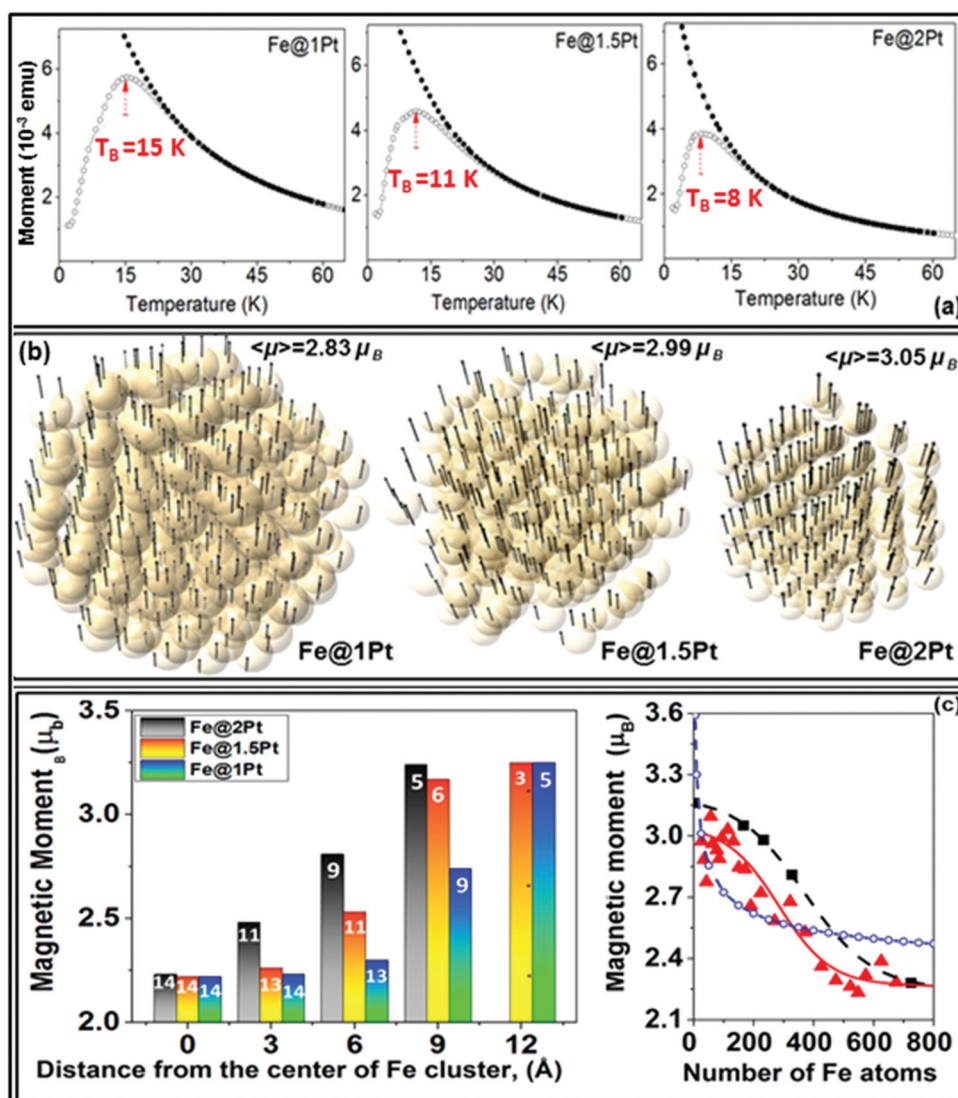

Fig. 4 (a) Temperature dependence of the zero field cooled (open circles) and field (100 Oe) cooled (filled circles) magnetization for Fe@Pt NCs. The blocking temperature, T_B, is given for each data set. (b) Atoms (circles) forming the Fe cores of Fe@Pt NCs. Arrows represent the magnetic moments of individual Fe atoms assessed for $T < T_B$ as explained in the text. The average magnetic moment per Fe atom, $<\mu(N)>$, in the respective cores is also given. (c) (left) $<\mu_R>$ (bars) and CN_{eff} (numbers inside the bars) as a function of the distance, R, from the center of Fe cores. (right) Experimental (red triangles),[43] 3D nanostructure-derived (black rectangles; see eqn (S6)†) and assumed (blue circles; see eqn (S27)†) $<\mu(N)>$ values as a function of the size of Fe cores/clusters comprising N atoms. Red solid and black broken lines are sigmoidal fits to the respective data sets (see eqn (S29)†). The blue line is a guide to the eye.

On grounds discussed in the ESI† (see eqn (S5)†) and using the experimental data for T_B, the effective magnetic anisotropy for Fe@1Pt, Fe@1.5Pt and Fe@2Pt NCs was estimated to be in the order of 9.2×10^5 J m^{-3}, 9.09×10^5 J m^{-3} and 9.04×10^5 J m^{-3}, respectively. The values are considerably larger than the magneto-crystalline anisotropy intrinsic to bulk bcc Fe (5.5×10^4 J m^{-3}) and, as shown in the work of others, can be attributed to the abrupt change in the coordination environment of atoms at the surface of cluster-like Fe cores, including surface relaxation effects.[29,30] Here it is to be added that the total magnetic moment of Fe clusters is composed from the magnetic moments of the constituent atoms and so can be many tens of μ_B, if not larger. The contribution of surface atoms to the total moment and large anisotropy of Fe clusters, including the evolution of that contribution with the cluster's size, though, is not well understood. Here we show that the missing knowledge can be provided by the streamlined 3d-band model theory based on ensemble-averaged positions of atoms forming the clusters.

Discussion

The ORR activity and superparamagnetic behavior of Fe@Pt NCs can be rationalized by evoking the generic features of the valence electron structure of Pt and Fe atoms constituting the NCs. In particular, the valence electron configuration of single Pt atoms is 5d^{9}6s^1. However, at the bulk scale, a small number of 5d-electrons are pushed into higher energy 6s and 6p states through a process known as (sp)–d hybridization, giving rise to the so-called 5d-holes. Hence, the actual valence electron configuration of bulk Pt is 5d$^{8.66}$6(sp)$^{1.34}$ Studies have found that the ORR activity of Pt surfaces is influenced strongly by the degree of (sp)–d hybridization, width, and energy position of the surface 5d-electron band, and occupied surface 5d-electron density of states (d-DOS).[4,31–33] On the other hand, when Fe atoms (3d^{6}4s^2) are brought together to form a solid, the valence 3d-electrons of Fe are distributed over the so-called majority (3d↑ spin-up) and minority (3d↓ spin-down) bands whereas valence 4s-electrons occupy a nearly half-empty 4(sp)-band. The majority and minority d-bands intersect the Fermi level and, due to strong (dd) and (sd) hybridization effects leading to the so-called 3d-holes, the magnetic moment of Fe atoms appears to be 2.2μ_B. Note that according to the so-called Hund's rules that moment is expected to be 3μ_B. For Fe clusters, this picture changes significantly because a large fraction of the atoms are on the surface and so have a reduced number of nearest neighbors. Accordingly, the 3d-electrons of surface Fe atoms are less delocalized, i.e. the width of both 3d↑ and 3d↓ bands diminishes. Besides, the energy position of 3d↑ and 3d↓ bands shifts with respect to the Fermi level and so the number of 3d-holes in the 3d↑ band is reduced. Ultimately, the magnetic moment of the surface atoms in Fe clusters approaches 3μ_B and the average magnetic moment per atom, <$\mu(N)$>, in the clusters may appear significantly larger than 2.2μ_B.[29,34,35]

As discussed in the ESI (see eqn (S23)–(S25)†), the width, energy position and occupancy of valence d-bands (d-DOS), i.e. the valence d-band structure, in the vicinity of atomic sites on the surface of transition (Fe) and noble (Pt) metals are largely determined by the local coordination of the sites, including the near neighbor distances and coordination numbers (CNs). Therefore, we used the so-called effective coordination numbers, CN$_{eff}$, to directly assess the atomic structure–function relationship for Fe@Pt NCs, where function pertains to applications involving superparamagnetic-type particles and ORR catalysts. The CN$_{eff}$'s were computed from the 3D positions of atoms in the RMC-refined structures of Fe@Pt NCs using eqn (S26).† Computational details are given in the ESI.† Here it is to be underlined that the approach of using CN$_{eff}$ instead of the traditional counting of near neighbors is similar to the embedded-atom method, where the valence electron density at an atomic site is approximated by a superposition of the valence electron densities of the nearby atoms that, in turn, are a superposition of the valence electron densities of the first neighbors for those atoms. Besides, the approach has already proved useful in describing the ORR activity of Pt surfaces and magnetic properties of low-dimensional Fe structures.[36–39] The so-obtained CN$_{eff}$'s for Pt atoms forming the top surface of Fe@Pt NCs and Fe atoms constituting the core of the NCs are summarized in Fig. 3d and 4c, respectively. Distribution of near-neighbor (bonding) distances for surface Pt atoms was also computed. It is shown in Fig. 3b in terms of the surface strain normalized against the bulk Pt–Pt distance of 2.775 Å.

As data in Fig. 3b show, Pt atoms forming the "skin" of Fe@1Pt NCs are significantly compressed (~1.2% on average), i.e. have come significantly closer together, as compared to surface atoms in pure Pt NCs. On average, top surface Pt atoms in Fe@1.5Pt and Fe@2Pt NCs also appear compressed, though to a lesser extent. On the other hand, on average, top surface atoms in pure Pt NCs are hardly compressed as compared to atoms on a perfect (111) facet of bulk Pt. We argue that the extra compressive strain of the Pt skin in Fe@Pt NCs is due to (i) the lack of structural coherence at the bcc-type Fe@fcc-type Pt interface and (ii) mismatch between the size of Fe and Pt atoms forming the NC core and skin, respectively. Experimental studies have shown and theory has predicted that, largely because of being favorable to the ORR changes in surface d-DOS and geometry, Pt surfaces compressed by 1% to 2% function as ORR catalysts better than unstrained Pt surfaces.[1,4,31,40] Hence, the observed here systematic increase in the atomic-level strain on the very surface of Fe@Pt NCs with the diminishing thickness of the Pt skin, that is ~0.2%, 0.8%, 1% and 1.2% surface strain for pure Pt, Fe@2Pt, Fe@1.5Pt and Fe@1Pt NCs, respectively, may well explain the observed trend in the ORR activity of the NCs. Note that considering the observed significant compression/shortening of the surface Pt–Pt bonding distances, i.e., increased d–d electron interactions, it may be conjectured that 6sp electrons of surface Pt atoms in Fe@Pt NCs would gain some 5d-character through sp → d charge redistribution (re-hybridization) and so the valence

electron configuration of the atoms would become more $5d^96(sp)^1$-like (vs. $5d^{8.66}6(sp)^{1.34}$ bulk configuration) with the increase in the size of the Fe core in the NCs. A somewhat increased occupation of the Pt 5d-band would lead to a decrease in the core-level binding energy for Pt atoms in Fe@Pt NCs, as indeed observed here (see Fig. 1c). Furthermore, effectively, the significant shortening of Pt–Pt bonding distances would lead to an increase in the average surface CN_{eff} for Fe@Pt NCs. In particular, when computed from the respective 3D structures, the number of 5- and 6-fold coordinated surface Pt atoms in Fe@1Pt, Fe@1.5Pt, Fe@2Pt and pure Pt NCs turns out to be 54%, 41%, 34% and 15% of all surface atoms, respectively. As exemplified in Fig. 3c, the relative increase in the surface CN_{eff} is most pronounced for atoms near the edges of the Pt skin whereas atoms at the edges largely remain under-coordinated, that is, 3- and 4-fold coordinated. According to the d-band center theory, bond order conservation arguments and experimental observations, higher coordinated sites on Pt surfaces are less reactive than low coordinated ones, in particular with respect to oxygen species, and so are likely to accelerate the ORR kinetics.[4,31,40,41] Remarkably, as data in Fig. 3d show, when normalized against the total number of Pt atoms in the respective NCs, the percentage increase in the surface CN_{eff} for Fe@Pt NCs with the decrease in the thickness of the Pt skin matches the enhancement factor in the ORR activity of the NCs obtained by our independent catalytic studies. The observation underlines the importance of incommensurate guest–host nanostructures, such as NCs, comprising a cluster-like core of Fe atoms nested inside a super-thin Pt skin, and relatively longer range surface coordination effects, as reflected in CN_{eff}'s, in tuning up the functionality of Pt-based catalysts for ORR. Also, it is a prime example of quantifying the structure–catalytic property relationship for metallic NCs on the basis of ensemble-averaged 3D positions of atoms in the NCs.[4,41] Note that prior DFT studies based on an idealized atomic-scale structure have indicated that the excellent catalytic performance of Fe@Pt NCs is likely due to surface structural distortions but did not quantify the exact relationship between the two.[13]

Using a streamlined 3d-band model for the magnetic properties of Fe clusters (see eqn (S6)†) and the respective CN_{eff}, we computed the magnetic moment, μ, for each Fe atom in the cores of Fe@Pt NCs, the average magnetic moment per Fe atom, $<\mu_R>$, as a function of the radial distance, R, from the center of the cores, and the average magnetic moment per Fe atom, $<\mu(N)>$, for each of the cores.[36,37] In the computations we used the experimental values for the magnetic moment of Fe atoms in bulk, $\mu_{Fe(bulk)} = 2.22\mu_B$ and of Fe–Fe dimers, μ_{Fe} (dimer) $= 3.25\mu_B$.[34,35] The 3D rendition of Fe cores in Fe@Pt NCs where each of the constituent atoms is assigned a magnetic moment computed as described above is shown in Fig. 4b. The evolution of $<\mu_R>$ with R is shown in Fig. 4c. As can be seen in the figures, atoms at the very center of the Fe cores have about 14 near neighbors and so carry the magnetic moment of bulk Fe atoms. Also, due to the gradual decrease in

the respective CN_{eff}'s, the closer the Fe atoms to the core surface the higher their magnetic moment. Notably, the magnetic moment of near-surface Fe atoms with ≤6 near neighbors approaches $3\mu_B$, which corresponds to a valence electron structure of $5(3d\uparrow)2(3d\downarrow)1(4s)$-type. Such a sharpening of Fe 3d-bands is consistent with the observed increase in the core-level binding energy for Fe atoms in Fe@Pt NCs with the decrease in the size of the NC's core (see Fig. 1a).

Also shown in Fig. 4c are computed values for $<\mu(N)>$ and experimental data, $<\mu(N)^{exp}>$, resulting from "Stern-Gerlach" type studies of Fe clusters.[42,43] Note that in deriving $<\mu(N)^{exp}>$ data, it has been assumed that the dependence of the magnetization for a superparamagnetic sample/ensemble of Fe clusters on the applied external magnetic field and temperature may well be approximated by the Langevin function (see eqn (S28)†). As can be seen in the figure, $<\mu(N)>$ obtained here and $<\mu(N)^{exp}>$ obtained elsewhere agree reasonably well. Indeed, considering that each $<\mu(N)^{exp}>$ data point appears as an average of the magnetic moments of a large ensemble of Fe clusters each comprising N atoms, the observed agreement may not come as a surprise. In particular, within the limits of a spherical cluster model (see eqn (S27)†), it may be conjectured that $<\mu(N)^{exp}>$ would evolve approximately as $N^{-1/3}$.[44] As can be seen in Fig. 4c though, the convergence of $<\mu(N)^{exp}>$ to the bulk value with increasing N is not as uniform and slow as conjectured on the basis of common knowledge. Somewhat more specific models envisioning that Fe clusters comprising a particular number of atoms ought to appear as a particular polyhedron or some of its derivatives, including truncated decahedron, cuboctahedron, rhombic dodecahedron and others, fail in describing the observed dependence of $<\mu(N)^{exp}>$ on N either.[44–47] We argue that, largely, the failure is due to ignoring the ensemble-average nature of $<\mu(N)^{exp}>$.[2] In particular, the foregoing models ignore the fact that, due to their intrinsically non-periodic nature, transition metal clusters with the same size (number of atoms N) may appear as an ensemble of various energetically degenerate isomers wherein corresponding atoms, in particular surface atoms, have somewhat different coordination environments and so carry a somewhat different magnetic moment.[44,48–50] As evidenced by data in Fig. 4c and elaborated in the ESI† (see eqn (S29)†), the cluster-size dependence of both $<\mu(N)^{exp}>$ and $<\mu(N)>$ obtained here may well be described by a sigmoid-type function that is strongly related to the Langevin function and, on a more general basis, to the so-called Boltzmann sigmoidal model. Notably, the latter, i.e. Boltzmann distribution, may well describe the statistical distribution of metallic NCs comprising the same number of (N) atoms over somewhat different structure states.[51–53] Altogether, when the ensemble-average nature of $<\mu(N)^{exp}>$ data resulting from "Stern-Gerlach" type experiments and $<\mu(N)>$ values derived from ensemble-averaged 3D atomic structure data is recognized not only do the latter ($<\mu(N)>$) appear as a true representation of the former ($<\mu(N)^{exp}>$) but also the long-debated dependence of ($<\mu(N)>$) on N can be described by a statistical theory for non-interacting superparamagnetic-type clusters. This is a prime example

of determining a fundamental relationship between the atomic-scale structure and functional properties of composite metallic NCs, in particular superparamagnetic properties, based on ensemble-averaged 3D positions of atoms constituting a structurally incommensurate component of the NCs.

Conclusions

Fluctuations in the size and shape of nanosized materials produced and used en masse, such as metallic NCs, can be significant and are hard to avoid. Besides, due to their cluster–bulk solid duality, NCs with the same size (N) and overall chemical composition are likely to appear as ensembles of near identical atomic configurations from a pool of possible structures, often referred to as a "structural landscape". Hence, even when under thermodynamic equilibrium conditions actual NCs are unlikely to adopt some "ground-state", *i.e.* lowest energy and so most stable, 3D atomic structure. Certainly, a greater stability of some atomic structure as compared to possible others would result in a greater probability of its occurrence but may not guarantee that the population of NCs with that structure in the respective ensemble would be predominant. That is, the typically large ensembles of metallic NCs explored for practical applications may be expected to exhibit some structural diversity and this phenomenon has to be taken into account by both theory and experiment for their accuracy to be improved.[2,49,53,54] Yet, regardless of their ensemble-average character, the salient structural features and physicochemical properties of metallic NCs produced with due care in pursuit of a given functionality would appear as durable macroscopic quantities. Indeed this is the reason behind the consistent functionality of metallic NCs in practical applications. As demonstrated here, the quantities, in particular the 3D positions of atoms in the NCs, can be measured with high precision by advanced X-ray scattering techniques. Moreover, new structure knowledge obtained can help not only reveal but also quantify the NC structure–function relationship, thereby enabling a rational design of better NCs.

Conflicts of interest

There are no conflicts to declare.

Acknowledgements

References

1 S. Shao, Q. Chang, J.-P. Dodelet and R. Chenitz, *Chem. Rev.*, 2016, **116**, 3594–3657.

2 X. Xu, Sh. Yin, Sh. R. Moro and W. A. de Heer, *Phys. Rev. B: Condens. Matter*, 2008, **78**, 054430–054413.

3 Q. A. Pankhurst, J. Connolly, S. K. Jones and J. Dobson, *J. Phys. D: Appl. Phys.*, 2003, **36**, R167–R181.

4 B. Hammer and J. K. Norskov, *Adv. Catal.*, 2000, **45**, 71–129.

5 R. Ferrando, J. Jellinek and R. L. Johnston, *Chem. Rev.*, 2008, **108**, 845–891.

6 I. Robinson and R. Harder, *Nat. Mater.*, 2009, **8**, 291–298.

7 Y. Yang, Ch. Chun, M. C. Scott, C. Ophus, P. A. Xu, L. Wu, F. Sun, W. Theis, J. Zhou, M. Eisenbach, P. R. C. Kent, R. F. Sabirianov, H. Zeng, P. Ercius and J. Miao, *Nature*, 2017, **542**, 75–79.

8 J. Miao, P. P. Ercius and S. J. L. Billinge, *Science*, 2016, **353**, 6306.

9 V. Petkov, *Mater. Today*, 2008, **11**, 28–38.

10 C. J. Hadjipanayis, M. J. Bonder, S. Balakrishnan, X. Wang, H. Mao and G. C. Hadjipanayis, *Small*, 2008, **4**, 1925–1929.

11 J. Ticek, Z. Sofer, D. Bousa, M. Pumera, K. Hola, A. Mala, K. Polakova, M. Navrodova, K. Cepe, O. Tomanec and R. Zboril, *Nat. Commun.*, 2016, **7**, 12879.

12 M. K. Debe, *Nature*, 2012, **486**, 43–51.

13 J.-H. Jang, E. Lee, J. Park, G. Kim, S. Hong and Y.-U. Kwon, *Sci. Rep.*, 2013, **3**, 2872.

14 H. P. Erickson, *Biol. Proced. Online*, 2009, **11**, 32–51.

15 M. Xue and Q. Guo, *Chem. Phys. Lett.*, 2012, **551**, 92–95.

16 T. Toda, H. Igarashi, H. Ucida and M. Watanabe, *J. Electrochem. Soc.*, 1999, **146**, 3750–3756.

17 B. R. Cuenya, L. K. Ono, J. R. Croy, A. Naitabdi, H. Heinrich, J. Zhao, E. E. Alp, W. Sturhahn and W. Keune, *Appl. Phys. Lett.*, 2009, **95**, 143103.

18 B. R. Cuenya, J. R. Croy, L. K. Ono, A. Naitabdi, H. Heinrich, W. Keune, J. Zhao, W. Sturhahn, E. E. Alp and M. Hu, *Phys. Rev. B: Condens. Matter*, 2009, **80**, 125412–125417.

19 Z. Bayindir, P. N. Duchesne, S. C. Cook, M. A. MacDonald and P. Zhang, *J. Chem. Phys.*, 2009, **131**, 244716–244717.

20 R. Cerny and V. Favre-Nicolin, *Z. Kristallogr.*, 2007, **222**, 105–113.

21 T. C. Monson, L. Venturini, V. Petkov, Y. Ren, J. M. Lavin and D. L. Huber, *J. Magn. Magn. Mater.*, 2013, **331**, 156–161.

22 W. Waseda, in *Anomalous X-Ray Scattering for Materials Characterization: Atomic-Scale Structure Determination*, Springer, Berlin, 2002.

23 S. Grazulis, D. Chateigner, R. T. Downs, A. F. T. Yokochi, M. Quiros, L. Lutterotti, E. Manakova, J. Butkus, P. Moeck and A.-L. Bail, *J. Appl. Crystallogr.*, 2009, **42**, 726–729.

24 W. B. Pearson, in *The crystal chemistry and physics of metals and alloys*, Wiley-INTERSCIENCE, New York, 1972.

25 V. Petkov, B. Prasai, Y. Ren, S. Shan, J. Luo, P. Joseph and Ch.-J. Zhong, *Nanoscale*, 2014, **6**, 10048–10061.

26 B. H. Toby and T. Egami, *Acta Crystallogr., Sect. A: Fundam. Crystallogr.*, 1992, **48**, 336–346.

27 B. E. Warren, in *X-ray Diffraction*, Addison-Wesley Publ. Co, 1969.

28 J. M. D. Coey, *Magnetism and Magnetic Materials*, Cambridge University Press, Cambridge, 2010.

29 D. L. Leslie-Pellecky and R. D. Rieke, *Chem. Mater.*, 1996, **8**, 1770–1783.

30 S. Oyarzu, A. Tamion, F. Tournus, V. Dupuis and M. Hillenkamp, *Sci. Rep.*, 2015, **5**, 14749.

31 V. Stamenkovic, B. S. Mun, M. Arenz, K. J. J. Mayrhofer, C. A. Lucas, G. Wang, P. N. Ross and N. M. Markovic, *Nat. Mater.*, 2007, **6**, 241–247.

32 J. K. Norskov, J. Rossmeisl, A. Logadottir, L. Lundkvist, J. R. Kitchin, T. Bligaard and H. Jonsson, *Phys. Chem. B*, 2004, **108**, 17886–17892.

33 V. Stamenkovic, B. S. Mun, K. J. J. Mayrhofer, P. N. Ross, M. N. Markovic, J. Rossmeisl, J. Greeley and J. K. Nørskov, *Angew. Chem., Int. Ed.*, 2006, **45**, 2897–2901.

34 *Advanced Magnetic nanostructures*, ed. D. J. Sellmyer and R. Skomski, Springer, 2005.

35 *Handbook of Magnetism and Advanced Magnetic Materials*, ed. H. Kronmüller and S. Parkin, Wiley, 2007, vol. 3.

36 D. Tomanek, S. Mukherjee and K. H. Bennemann, *Phys. Rev. B: Condens. Matter*, 1983, **28**, 665–673.

37 J. Zhao, X. Chen, Q. Sun, F. Liu and G. A. Wang, *Phys. Lett. A*, 1995, **205**, 308–312.

38 X. Ma and H. Xin, *Phys. Rev. Lett.*, 2017, **118**, 036101–036105.

39 F. Calle-Vallejo, J. Tymoczko, V. Colie, Q. H. Vu, M. D. Pohl, K. Morgenstern, D. Loffreda, Pf. Sautet, W. Schuhmann and A. S. Bandaenka, *Science*, 2015, **350**, 185–189.

40 J. H. Wang, H. Inada, L. Wu, Y. Zhu, Y. Choi, P. Liu, W.-P. Zhou and R. Adzic, *J. Am. Chem. Soc.*, 2009, **131**, 17298–17302.

41 B. C. Han, C. R. Miranda and G. Ceder, *Phys. Rev. B: Condens. Matter*, 2008, **77**, 075410–075419.

42 I. M. L. Billas, J. A. Becker, A. Chatelain and W. A. de Heer, *Phys. Rev. Lett.*, 1993, **71**, 4067–4070.

43 I. M. L. Billas, A. Chatelain and W. A. de Heer, *Science*, 1994, **265**, 1682–1684.

44 J. A. Alonso, *Chem. Rev.*, 2000, **100**, 637–677.

45 F. Aguilera-Granja, J. M. Montejano-Carrizales and J. L. Moran-Lopez, *Phys. Lett. A*, 1998, **242**, 255.

46 N. A. Besley, R. L. Johnson, A. J. Stace and J. Uppenbrink, *J. Mol. Struct.*, 1995, **341**, 75–90.

47 O. Sipr, M. Kosuth and H. Ebert, *Phys. Rev. B: Condens. Matter*, 2004, **70**, 174423–174413.

48 In general, isomers are compounds with the same chemical composition that are structurally different in some way.

49 V. Petkov, N. Bedford, M. R. Knecht, M. G. Weir, R. M. Crooks, W. Tang, G. Henkelman and A. Frenkel, *J. Phys. Chem. C*, 2008, **112**, 8907–8911.

50 Z. Li, N. F. Young, M. di Vece, S. Palomba, R. E. Palmer, A. L. Bleloch, B. C. Curley, R. L. Johnston and J. Yuan, *Nature*, 2008, **451**, 46–48.

51 F. Reif, in *Fundamentals of Statistical and Thermal Physics*, McGraw–Hill, 1965.

52 L. J. Reed and J. Berkson, *J. Phys. Chem.*, 1929, **33**, 760–779.

53 A. S. Barnard, *Nanoscale*, 2014, **6**, 9983–9990.

54 K. K. Jha, S. Dutta, V. Kumar and P. Munshi, *CrystEngComm*, 2016, **18**, 8497–8505.